# Journal Pre-proof

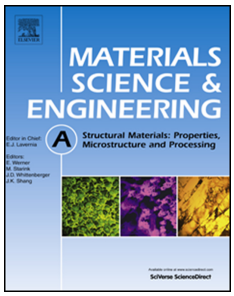


Laser powder bed fusion of advanced submicrometer $TiB_2$ reinforced high-performance Ni-based composite

Zhenhua Zhang, Quanquan Han, Shengzhao Yang, Yingyue Yin, Jian Gao, Rossitza Setchi

PII: S0921-5093(21)00685-7

DOI: https://doi.org/10.1016/j.msea.2021.141416

Reference: MSA 141416

To appear in: *Materials Science & Engineering A*

Received Date: 5 February 2021

Revised Date: 17 April 2021

Accepted Date: 4 May 2021

Please cite this article as: Z. Zhang, Q. Han, S. Yang, Y. Yin, J. Gao, R. Setchi, Laser powder bed fusion of advanced submicrometer $TiB_2$ reinforced high-performance Ni-based composite, *Materials Science & Engineering A*, https://doi.org/10.1016/j.msea.2021.141416.

## CRediT authorship contribution statement

**Zhenhua Zhang:** Conceptualization, Methodology, Writing-original draft. **Quanquan Han:** Conceptualization, Investigation, Writing - Original Draft, Funding acquisition. **Shengzhao Yang:** Resources, Writing - Review & Editing. **Yingyue Yin：**Visualization, Data curation. **Jian Gao:** Software, Investigation. **Rossitza Setchi:** Methodology, Review & Editing.

# Laser powder bed fusion of advanced submicrometer $TiB_2$ reinforced high-performance Ni-based composite

**Zhenhua Zhang [a,b], Quanquan Han [a,b*], Shengzhao Yang[a,b], Yingyue Yin[a,b], Jian Gao[a,b], Rossitza Setchi[c]**

[a]Key Laboratory of High Efficiency and Clean Mechanical Manufacture of Ministry of Education, Center for Additive Manufacturing, School of Mechanical Engineering, Shandong University, Jinan, 250061, China

[b]Key National Demonstration Center for Experimental Mechanical Engineering Education, Shandong University, Jinan, 250061, China

[c]Cardiff School of Engineering, Cardiff University, Cardiff, CF24 3AA, UK

**Corresponding author**:

Quanquan Han, Hanquanquan@sdu.edu.cn, +86531-88392608

## Abstract

The Ni-based Hastelloy X (HX) superalloy is widely used in aero-engine components because of its exceptional high-temperature strength and oxidation resistance. Given the complex structure of such parts, additive manufacturing (AM) technologies such as laser powder bed fusion (LPBF) are employed to manufacture these components. HX alloy suffers from crack susceptibility during the LPBF process, however. In this paper, this issue was addressed by adding 2 wt.% submicrometer $TiB_2$ powder through a high-speed mixing process. Both the low-angle grain boundaries (LAGBs) and high-angle grain boundaries (HAGBs) were noted to have increased in the as-fabricated HX-2 wt.% $TiB_2$ composite, with an average grain size reduction from 14 μm to 8.69 μm. In addition, compared with pure HX, the hardness of the HX-2 wt.% $TiB_2$ composite was increased by 43.4% and 50.8% at room-temperature and high-temperature (850°C) conditions, respectively. This indicates that the added $TiB_2$ reinforcement was more influential to the mechanical property enhancement under high-temperature compared to the room temperature conditions. The composite sample also showed a 28% increase in yield

strength while the ductility was not found to be sacrificed compared to the as-fabricated pure HX, indicating that an addition of specific ceramic particles with suitable content may offer a new method for manufacturing crack-free high-strength and high-toughness HX alloy through the AM process. These findings also provide a reference for improving the properties of other advanced materials made by the LPBF process.

**Keywords:** Ni-based alloy; additive manufacturing; laser powder bed fusion; composite; cracking

## 1 Introduction

Hastelloy X (HX) is a Ni-based superalloy with Cr, Fe and Mo as solid solution strengthening elements. The matrix of HX superalloy is austenitic phase, while the carbides get enriched at the grain boundaries after subsequent heat treatments to further improve the mechanical performance [1]. As a typical high-temperature superalloy, HX exhibits exceptional combination of oxidation resistance, corrosion resistance and strength under high temperature conditions [2][3], enabling its working temperature reach around 900 °C. For these reasons, HX is suitable for manufacturing high-temperature parts such as engine combustion chambers and other high-temperature components [4]. But such parts are generally complex in structure and require high precision. The demands of processing rule out traditional processing methods such as forging, casting and milling [5].

Laser powder bed fusion (LPBF) is a rapidly developed metal additive manufacturing (AM) technology that is suitable for manufacturing metallic parts with complex geometries [6][7][8]. The process starts by slicing the 3D CAD file data into layers, usually from 20 to 100 micrometers thick, creating a 2D image of each layer; thin layers of fine metal powder are evenly distributed using a coating mechanism onto a substrate. Once each layer has been distributed, each 2D slice of the part geometry is fused by selectively

melting the powder. This is accomplished with a high-power laser beam, usually an ytterbium fibre laser with hundreds of watts. The laser energy is intense enough to permit full melting of the particles; the process is repeated layer by layer until the part is complete [9]. The extremely high cooling rate (around $10^7$ K/s) during the high-speed laser scanning process leads to the generation of residual thermal stress in the workpiece, which may cause cracking. This kind of cracking is known as hot cracking [5]. HX is a typical Ni-based alloy that is prone to cracking, and many studies have shown that the method of optimising LPBF process parameters cannot eliminate cracking within HX manufactured by LPBF [10][11][12][13][14].

Previous research [15] has shown that cracking in the process of LPBF-manufactured HX occurs for two main reasons. First, the carbides cannot completely dissolve in the matrix during the rapid heating and melting process. They might be distributed on the grain boundaries, and the melting point of the carbides is lower than the matrix, thus leading to the formation of liquid films [3][15]. Second, with the accumulation of residual thermal stress between layers, the carbide liquid film between grains is pulled apart by the residual stress to form intergranular cracks. Harrison et al. [16] found that the number of hot cracks could be reduced by adjusting the content of Mn and Si in the alloy, and the tensile strength could be improved at high temperatures (1033 K), but the cracks could not be eliminated. Inspired by the addition of zirconium particles to improve strength and eliminate LPBF-fabricated 6000 and 7000 series aluminium alloys [17] , an investigation of the effects of specific reinforcement phases on LPBF of HX alloy-based composites presents an interesting line of research.

Previous studies have shown that the addition of ceramic particles can improve the tensile strength, wear resistance and hardness of LPBF manufactured metal matrix composites (MMCs) [18][19][20]. For this reason, many scholars have researched the fabrication of particle-reinforced MMCs by LPBF. For instance, Zhang et al. [21] studied the microhardness and

microstructure evolution of samples after adding micron-size $TiB_2$ particles to Inconel 625 and found that the microhardness was greatly improved and that the microstructure was also significantly changed after adding $TiB_2$ particles. Zhao et al. [22] studied TiN/AISI 420 stainless steel composites manufactured by LPBF and found that the microhardness of 420 stainless steel powder increased by 11.8% after the addition of TiN particles; the wear resistance was also improved. Wang et al. [23] found that the mechanical properties of Inconel 625 were improved after the addition of carbon nanotubes.

Notably, the above researchers all revealed that the addition of reinforcing particles led to improved heterogeneous nucleation and grain refinement, thus indicating that grain refinement strengthening is among the main contributors to improved mechanical properties such as tensile strength.

The selection of reinforcing particles in the above studies was based more on experience than on theoretical guidance. According to the heterogeneous nucleation theory proposed by Turnbull and Vonnegut [24], the melting point of the nucleating agent is generally higher than the temperature of the matrix and exhibits stability in the liquid phase. The mismatch between the nucleating agent and the matrix must be very low in low-index surfaces. TiC particles were selected in the previous studies [25][11][26], which eliminated the micro cracking in LPBF-manufactured HX and greatly improved the tensile strength at room temperature.

However, TiC is easily oxidised above 600 °C [27], this temperature is generally lower than the working temperature of HX superalloy components (up to 900 °C). $TiB_2$ ceramic material is an ultra-high-temperature ceramic with a melting point over 3000 °C; it has a hexagonal crystal structure and exhibits excellent mechanical, thermophysical and chemical properties [28]. $TiB_2$ is thus considered to be an ideal reinforcement phase for exploring the role and strengthening mechanisms of ceramic particles on MMCs [29][30][31]. In addition, the planar disregistry between $TiB_2$ and nickel was similar to the disregistry between TiC and nickel, while $TiB_2$ offers a much higher oxidation

resistance (above 1100 °C) compared to TiC particles, which means that $TiB_2$ is more suitable for high-temperature applications in the aero-engine domain if the microcracks could also be mitigated in the LPBF fabricated HX-$TiB_2$ composite.

In this context, the present study has investigated the effects of 2 wt.% submicrometer $TiB_2$ particles on the microstructure and mechanical properties of LPBF-manufactured HX-$TiB_2$ composites under both room-temperature and high-temperature conditions. In particular, the $TiB_2$ particles' mechanism for crack mitigation was also studied.

## 2 Material and methods

### 2.1 $TiB_2$ particle selection

The raw HX-2 wt.% $TiB_2$ composite powder consisted of 98 wt.% commercial HX and 2 wt.% submicrometer $TiB_2$ particles. The main reason for choosing the $TiB_2$ particles to be the enhanced material was that $TiB_2$ has lower planar disregistry with a nickel lattice structure compared to other commonly used nucleating agents, such as WC, ZrC and SiC. According to the heterogeneous nucleation theory proposed by Turnbull and Vonnegut [24] , the effectiveness of a nucleating agent in promoting heterogeneous nucleation depends on the crystallographic disregistry between the nucleating agent and the nucleated solid. The disregistry proposed by Turnbull and Vonnegut [24] can be expressed as $\delta = (\Delta a_0 / a_0)$, where $\Delta a_0$ is the difference between the lattice parameter of the nucleating agent and the nucleated solid for a low-index plane; $a_0$ is the lattice parameter for the nucleated phase. The smaller the calculated disregistry factor, the better the heterogeneous nucleation effectiveness that is achieved between the nucleating agent and the nucleated solid. Because the formula proposed by Turnbull and Vonnegut [24] only applies to the calculation of crystals with similar structures, Bramfitt [32] improved the formula. The modified planar disregistry can be expressed as:

$$\delta_{(\mathrm{hkl})\mathrm{n}}^{(\mathrm{hkl})\mathrm{s}} = \frac{1}{3}\sum_{i=1}^{3}\frac{\left|\left(d[uvw]_s^i cos\theta\right) - d[uvw]_n^i\right|}{d[uvw]_n^i} \times 100$$

where (hkl)s and (hkl)n are the low-index crystallographic planes of nucleating agent $TiB_2$ and nickel, respectively, and [uvw]s and [uvw]n are the low-index directions in the (hkl)s and (hkl)n planes, respectively. The distance between the corresponding crystals and adjacent atoms is represented by d[uvw]s and d[uvw]n, respectively.

In this study, $TiB_2$ had a hexagonal lattice structure, while nickel had a face-centred-cubic structure. The calculated planar disregistry between $TiB_2$ and nickel was 21.9%. The planar disregistry between TiC and nickel was 20.9% studied by Han et al. [25]. Their study has revealed that TiC nanoparticles functioned as heterogenous nucleation sites and played a significant role in LPBF of high-performance nickel alloy. Although TiC and $TiB_2$ had different types of crystallographic structures, the two inclusion materials exhibit similar planar disregistry values with nickel. Therefore, $TiB_2$ particles may also play a significant role in promoting nucleation within LPBF of Ni-based HX composites. Compared to TiC ceramic material, however, $TiB_2$ exhibited improved high-temperature strength and oxidation resistance, making it a more suitable reinforcement phase for the LPBF of HX-based composite. Investigating the effects of $TiB_2$ particles on both the microstructure and mechanical properties of LPBF-manufactured HX composites is thus an interesting endeavour.

### 2.2 Feedstock preparation

The original Hastelloy X (HX) powder used in this study was a commercial powder produced by Praxair (Indianapolis, IN, USA) with a nominal particle size in the range of 16–45 μm (average particle size 30 μm). The powder's constituent element content was (wt.%) 21.58Cr-18.86Fe-8.9Mo-1.5Co-0.64W-0.2Si-0.08C-0.01Ti-0.01Mn-Bal. As shown in Fig. 1a, most of the particles showed notable sphericity, with a small

fraction of ellipsoidal and irregular powders; these irregular particles were not considered to have a large impact on powder flowability. $TiB_2$ powder with an average particle size of 600 nm was supplied by Cwnano (Shanghai, China). The submicrometer $TiB_2$ particles exhibited strong agglomeration and irregular shapes, which needed to be separated uniformly among the HX alloy. Several $TiB_2$ particles were also noted to have a size greater than 1 μm (Fig. 1b).

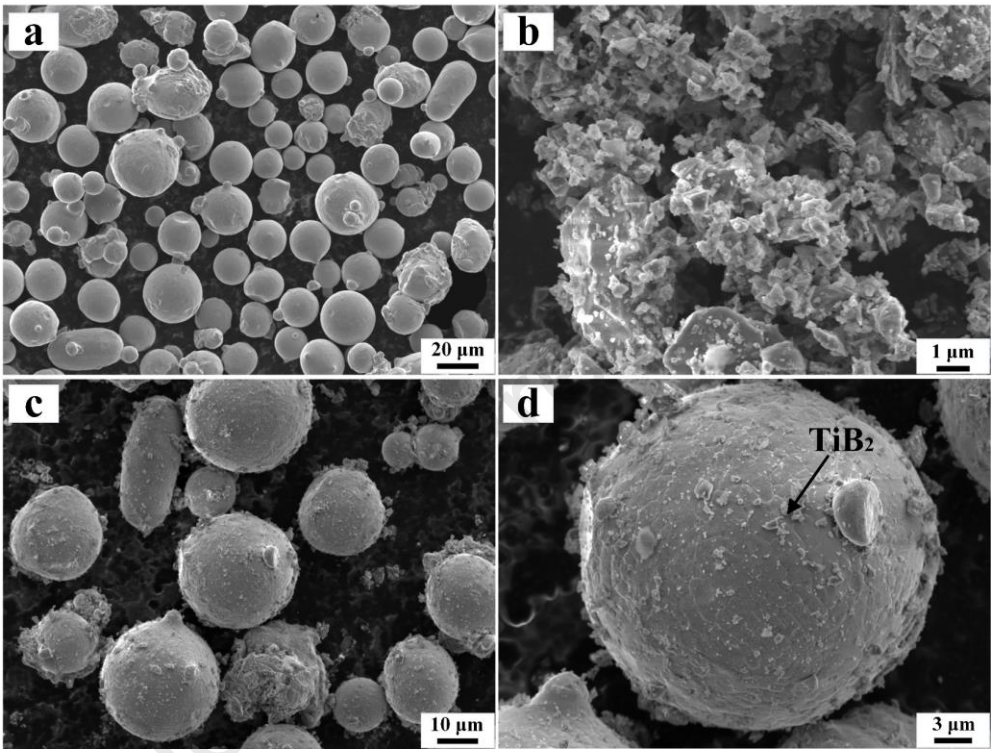


**Fig. 1.** Scanning electron microscopy (SEM) images of powder materials used in this study: (a) pure Hastelloy X (HX) powder; (b) submicrometer $TiB_2$ particles; (c) HX-2wt.% $TiB_2$ composite feedstock; (d) high-magnification SEM image of HX-2wt% $TiB_2$ composite powder; the arrow indicates the $TiB_2$ attached to the surface of the HX powder.

The original HX powder and $TiB_2$ powder were mixed at 1200 rpm using a high-speed mixer model DAC-800 (SpeedMixer, Nordrhein-Westfalen, Germany) to prepare the HX-2 wt.% $TiB_2$ raw material (composite feedstock). The HX powder and $TiB_2$ powder were first mixed at 1200 rpm for 2.5 minutes; the powder was then cooled to room temperature and again mixed for 2.5 minutes. As Figs. 1c and d show, the $TiB_2$ particles were evenly distributed on the surface of the original HX alloy.

### 2.3 Laser powder bed fusion process

A laser powder bed fusion (LPBF) machine, LATEC PBF-150 (LATEC, Jinan, China), with a laser power of 200 W, was used for the manufacture of pure HX and HX-2 wt.% $TiB_2$ composite samples in this study.

Both cubic samples (10×10×8 $mm^3$) and tensile samples were processed in the present work. The cubic samples were used to optimise the typical parameters, such as scanning spacing and scanning speed. The optimal parameters were selected by measuring the relative density of the cubic samples with different processing parameters. Therefore, the tensile samples were formed according to the optimal parameters that had been selected and were manufactured horizontally. The horizontal manufacture scenario indicates that the build direction is perpendicular to the tensile loading direction, while the vertical manufacture means that the build direction is parallel to the tensile loading direction. Previous studies have revealed that the build directions had a significant influence on tensile properties; the horizontally fabricated tensile components generally exhibit higher tensile strength with lower elongation values compared to the specimens fabricated by vertical manufacture scenarios [33][34]. In this study, both laser scanning speed and hatch spacing parameters were optimised while maintaining the other main manufacturing parameters (laser power = 200 W; layer thickness = 40 μm; scanning strategy = chessboard; rotation angle between any two layers = 67°).

### 2.4 Materials characterisation

The microstructure of the samples was characterised by scanning electron microscopy (SEM) and optical microscopy (OM). The cubic samples were cut by wire cutting parallel to the build direction; the section was then polished followed by sandpapering with 320, 600, 1500 and 2500 mesh SiC sandpaper. The samples were then polished with diamond polishing suspensions of 3 μm and 1 μm; finally, the samples were polished with 0.04 μm $SiO_2$ polishing

suspensions.

To observe the microstructure of the melt pool and the rapid solidification structure, the polished sample was electrochemically etched in a 10% oxalic acid solution for 20 s with a voltage of 7 V; high-resolution SEM micrographs and electron backscattered diffraction (EBSD) data were taken by a JSM-7800F (JEOL, Japan) field emission scanning electron microscope (FESEM) equipped with an EBSD probe model NordlysMax$^3$ (Oxford Instruments, Oxford, UK) and an XMax-80 device (Oxford Instruments, Oxford, UK).

In this study, the acceleration voltage of EBSD scanning was 20 kV, the scanning area was 800×800 μm$^2$ and the step distance was fixed at 1 μm. The EBSD data were processed using the HKL Channel 5 software package to generate grain boundaries and grain size information. The ion milling equipment (Gatan 695, Pleasanton, CA, USA) was used for specimen pre-treatment before transmission electron microscopy (TEM) inspection. TEM inspection was performed with the FEI F200X TALOS (FEI, Massachusetts, MA, USA) to further investigate the microstructure of the pure HX and HX-2 wt.% $TiB_2$ composite samples.

**2.5 Mechanical characterisation**

A microhardness tester model HVS-1000a (HUAYUZHONGXIN, Laizhou, China) was used for the room-temperature hardness measurement. The load was fixed at 200 g with a dwell time of 10 s. Five measurements were conducted and averaged to obtain the average microhardness value. A high-temperature Vickers hardness test system (model HTV-PHS30, London, UK) was employed to measure the high-temperature (850 °C) hardness of the two materials. To prevent oxidation, the samples were tested under the protection of an argon gas environment. Before the test, the temperature was raised to 850 °C gradually and then held for 5 min. The load was set to 1 kg,

with a dwell time of 10 s.

Uniaxial tensile testing was performed using a microcomputer-controlled electronic universal testing machine (FBS-100KNW, FBS, Shenzhen, China) with a strain rate of 1.33 x $10^{-3}$ $s^{-1}$ at room temperature. Two tensile specimens were tested for both conditions (pure-HX and HX-2 wt.% $TiB_2$ composite). The yield strength, ultimate tensile strength (UTS) and elongation were obtained by averaging the data from the two experiments.

# 3 Results

## 3.1 Defect evolution

Figs. 2a–b show the different relative densities of pure HX and HX-2 wt.% $TiB_2$ composite samples under different laser energy density values. The relative density was measured based on the Archimedes principle, and each point in the curve was tested three times and averaged. The energy density was calculated according to the primary process parameters, including laser power (P), scanning speed (V), hatch spacing (H), and powder layer thickness (T); the Energy Density is expressed as $\varepsilon = \frac{P}{V*H*T}$ [35].

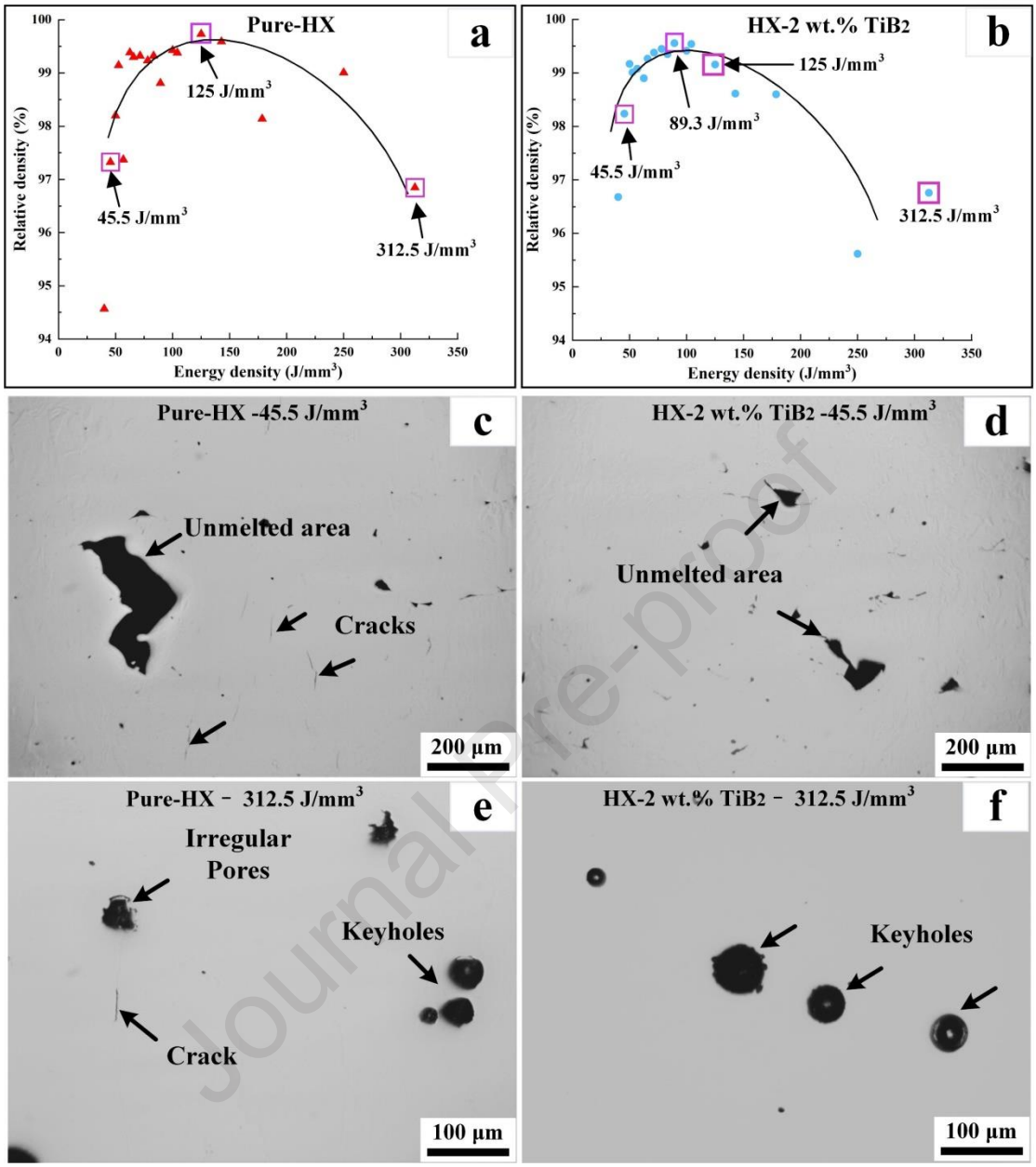


**Fig. 2.** Defect evolution in the as-fabricated samples: (a)–(b): measured relative density versus laser-energy density for pure and HX-2 wt.% $TiB_2$ composite samples; (c)–(f): optical microscopy (OM) images of pure HX and HX-2 wt.% $TiB_2$ composite under different laser-energy densities.

As Figs. 2a–b illustrated, both pure HX and composite samples showed a trend where the relative density of the sample increased at the beginning and then decreased with increased energy density. A higher relative density of the sample generally indicated fewer internal defects and higher processing quality. When a relatively low laser-energy density was employed (Figs. 2c-d), the unmelted area was the main defect in both samples. The unmelted area fraction in pure HX and composite samples was found to 3.15% and 1.58% (5

images considered for both cases), respectively. When a higher energy density was used, the keyhole pores were the major defect in both samples. The fraction of keyholes in pure HX and composite samples was 2.07% and 2.73% (5 images considered for both cases), respectively. It should be noted that, micro-cracks formed in pure HX under all the employed processing conditions and their formation was independent on the laser energy density. Since a highest relative density normally indicates a minimum defect fraction and best mechanical performance for the specimen, so the optimal processing parameters for pure HX in present study refers to the as-fabricated HX with the highest relative density and minimum defect fraction.

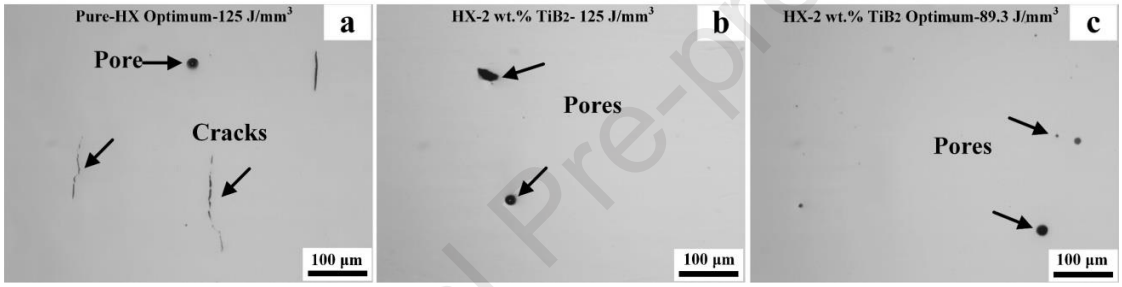


**Fig. 3.** Defect evolution in the as-fabricated samples: (a)–(b): optical microscopy (OM) images of pure HX and HX-2 wt.% $TiB_2$ composite under different laser-energy densities.

In pure HX (Fig. 2a), when the laser-energy density reached 125 J/mm$^3$, the relative density of the sample was the highest, which was measured to be 99.7%. Therefore, 125 J/mm$^3$ (scanning speed = 500 mm/s; hatch spacing = 80 µm) was considered the optimal processing parameter of pure HX, while the optimal energy density for the HX-2 wt.% $TiB_2$ composite was 89.3 J/mm$^3$ (scanning speed = 700 mm/s; hatch spacing = 80 µm), with a 99.6% relative density (Fig. 2b).

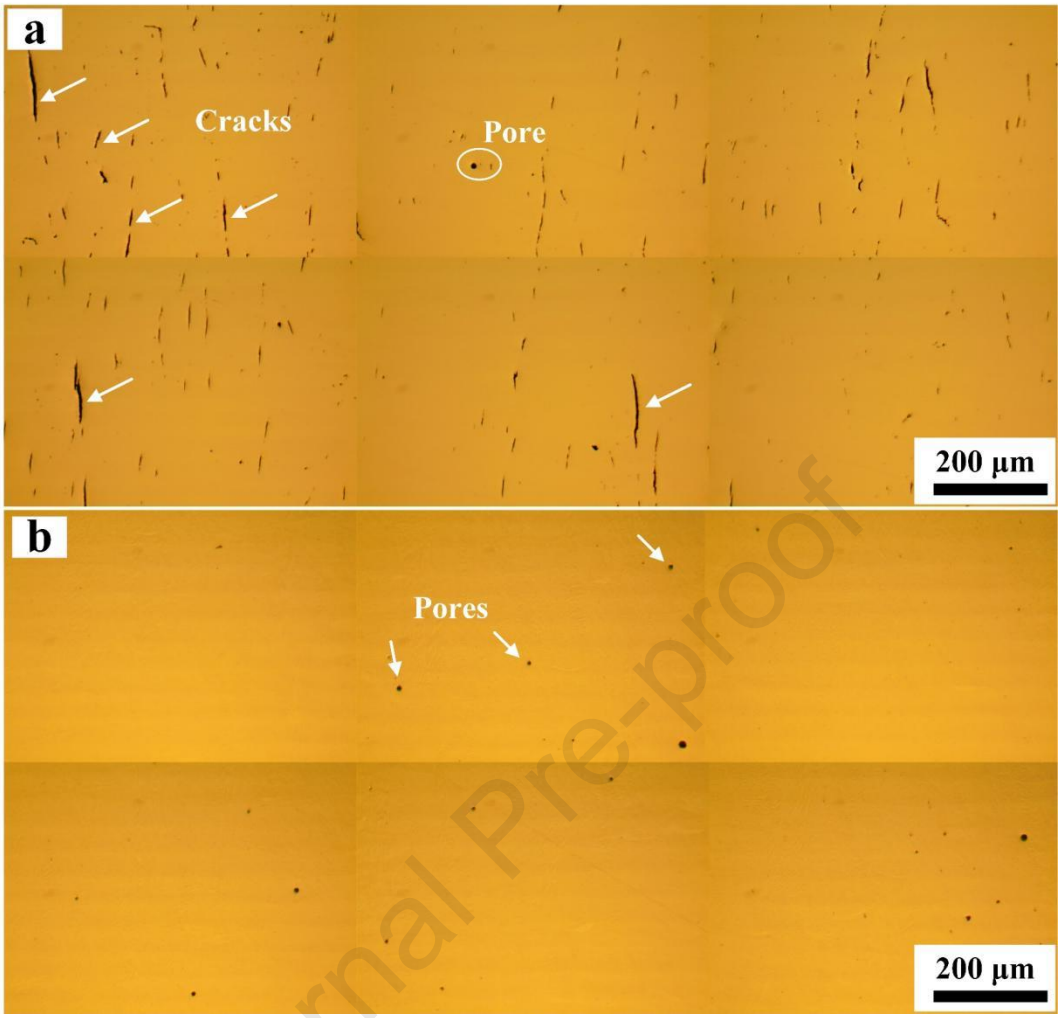


**Fig. 4.** Defect distribution for the two samples: (a) defects of pure HX under optimum energy density; (b) defects of HX-2 wt.% $TiB_2$ composite under optimum energy density.

OM images (Figs. 3a and 4a) showed that even under the optimal laser-energy density (125 J/mm$^3$), numerous microcracks were formed in the as-fabricated pure HX sample. Under the optimal laser-energy density (89.3 J/mm$^3$) of the composite sample, in contrast, no microcracks were detected under the OM inspection (Figs. 3c and 4b), although a few pores still existed. To further confirm that the elimination of cracks was not caused by the change of process parameters, the composite sample processed under 125 J/mm$^3$ laser-energy density was also characterised (Fig. 3b). Microcracks were also not detected, thus indicating that the elimination of cracks was induced by the addition of $TiB_2$ instead of the process parameters.

It should be noted that although the addition of $TiB_2$ managed to eliminate the microcracks in the samples, doing so could not stop the generation of pore defects; moreover, with the increase in energy density, the number of pores increased. Some pores were associated with deep and narrow vapour depressions called keyhole pores [36], which were larger than the open pores (Fig. 4b). Interestingly, although the high-density laser energy led to the generation of several keyhole defects in the composite sample, no cracks were noted in it, thus implying that the addition of $TiB_2$ could also suppress the generation of cracks under non-optimal manufacturing parameters.

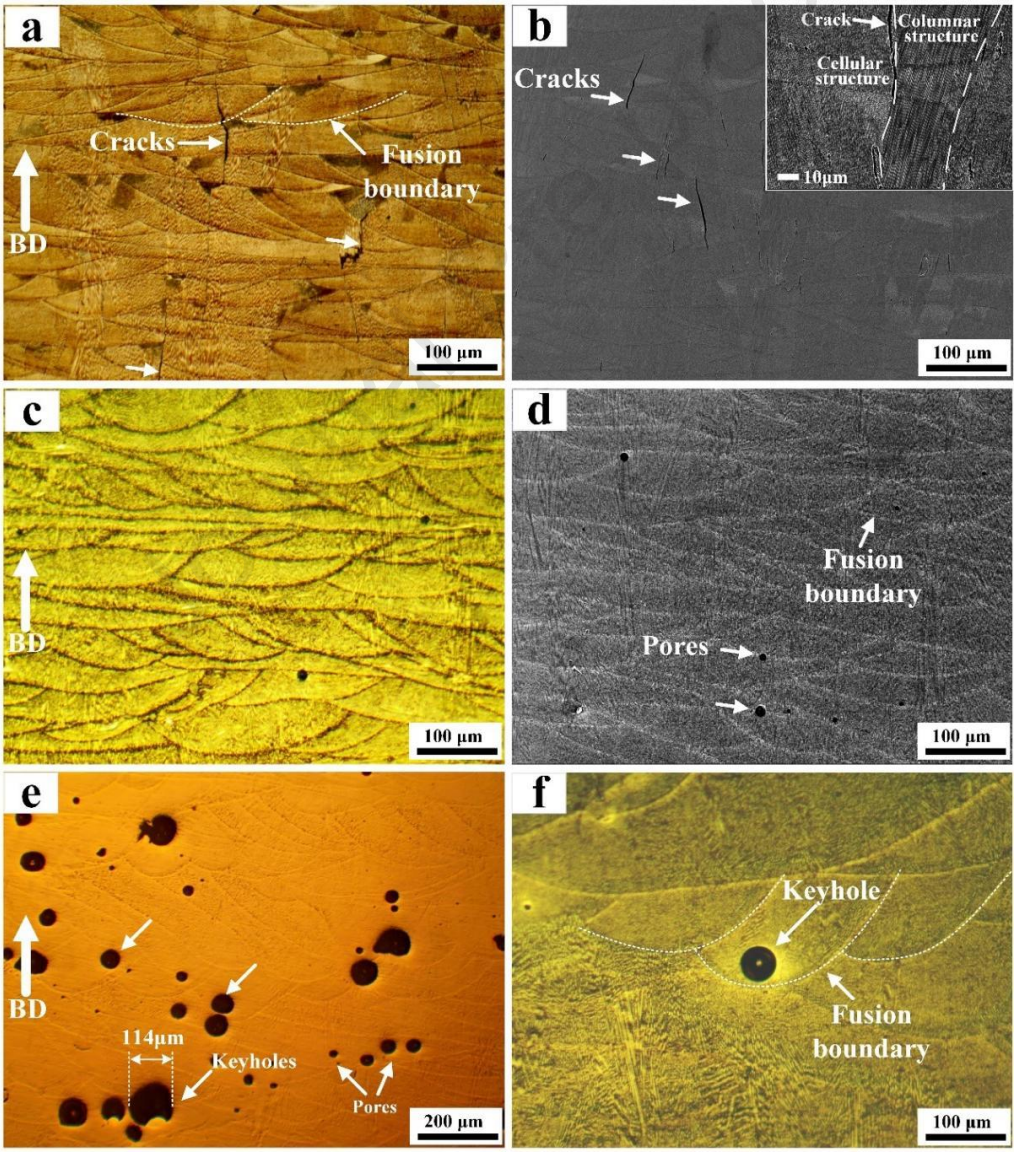


**Fig. 5.** Microstructure of pure HX and HX-2 wt.% $TiB_2$ composite samples after etching; (a)–(b): pure HX under optimum laser-energy density; (c)–(d): HX-2 w.t% $TiB_2$ under optimum laser-energy density; (e)–(f): HX-2 wt.% TiB2 composite sample under 312.5 J/mm3 laser-energy density.

Fig. 5 shows the molten pools and microstructure of pure HX and composite samples after electrochemical etching. As the figure shows, the cracks in pure HX grew across multi-layer molten pools along the build direction, and the crack length was more than 100 μm (Figs. 5a–b). The cracks were found to be intergranular, without trans-granular cracks forming, which is investigated in the next section. The fusion boundary morphology and microstructure of the composite sample formed under the optimal process parameters were similar to the pure HX (Figs. 5c–d), but more tiny open pores formed. Previous research has shown that the reinforced ceramic particles led to an increase in the viscosity of the molten pool [37]. With an increase in viscosity, the fluidity of the molten material decreased, which may mitigate the escape of gases from the molten pool. Therefore, the formed open pores may be partially attributed to the increase in molten pool viscosity caused by the addition of $TiB_2$ particles. With increased laser-energy density, the pore diameter reached more than 100 μm (Figs. 5e–f), which became a typical keyhole pore, thus indicating that the formation of keyhole defects was mainly related to laser-energy density.

### 3.2 Microstructure and phase identification

Fig. 6 shows the TEM energy-dispersive X-ray spectroscopy (EDX) mapping of the pure HX and HX-2 wt.% $TiB_2$ composite samples under the optimal LPBF conditions. Ti and B elements were not found in the pure HX sample by EDX (Fig. 6a). The EDX shows nanometric domains enriched in Ti element, and these domains are uniformly distributed in the matrix of HX-2 wt.% $TiB_2$ composite sample (Fig. 6b). This finding indicates the $TiB_2$ particles were uniformly distributed in the HX-2 wt.% $TiB_2$ composite without an apparent chemical reaction occurring between $TiB_2$ and the matrix.

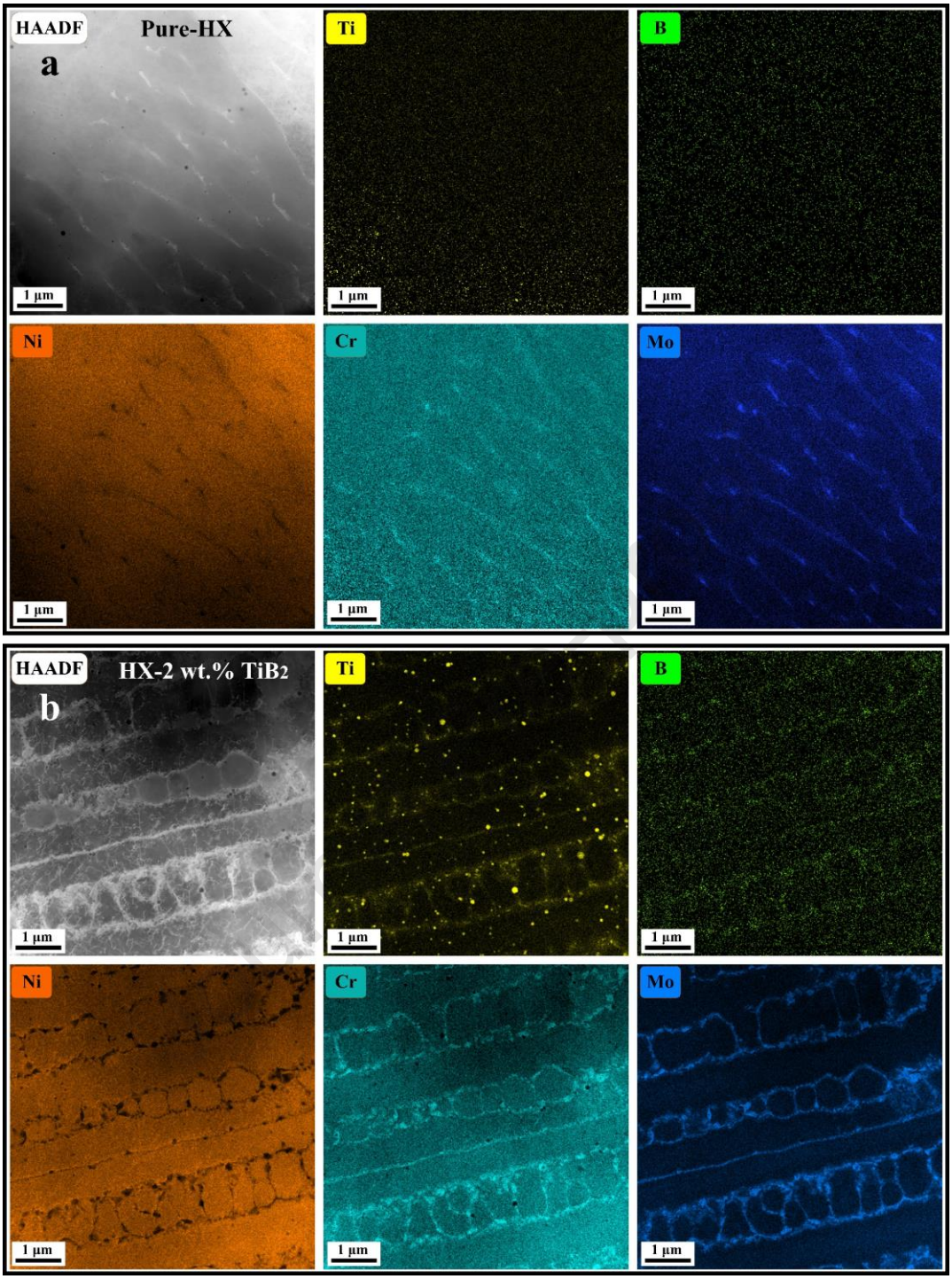


**Fig. 6.** Energy-dispersive X-ray spectroscopy (EDX) mapping; (a) the pure HX sample; (b) the HX-2 wt.% $TiB_2$ composite sample.

In addition, the Cr and Mo elements were enriched around the columnar walls both in the pure HX and composite samples, thus showing agreement with previous studies where Cr and Mo enriched carbides were also found in pure HX produced by LPBF [3][25] . Because the melting point of this kind of carbide is lower than the matrix, the liquid film might have formed during the

solidification stage; the liquid film could have been pulled apart by residual stress, with cracks then forming. Figs. 7a-b show the distribution of dislocations and precipitates in the as-fabricated pure HX and composite samples, respectively. The dislocation density in the composite was higher than that of pure HX sample. This situation may be attributed to the difference in the coefficient of thermal expansion between $TiB_2$ and the matrix, which caused the lattice deformation of austenitic matrix so that dislocations increased in the as-fabricated composite sample. The EDX point analysis was used to further confirm the composition of the precipitate in pure HX sample (Figs. 7c-d). The EDX results show the irregular precipitates were rich in Mo and Cr elements, while the C element content (about 3.72 wt.%) was much higher than the matrix (around 0.94 wt.%). This finding suggests that the formed precipitates were typical Cr and Mo enriched carbides [1].

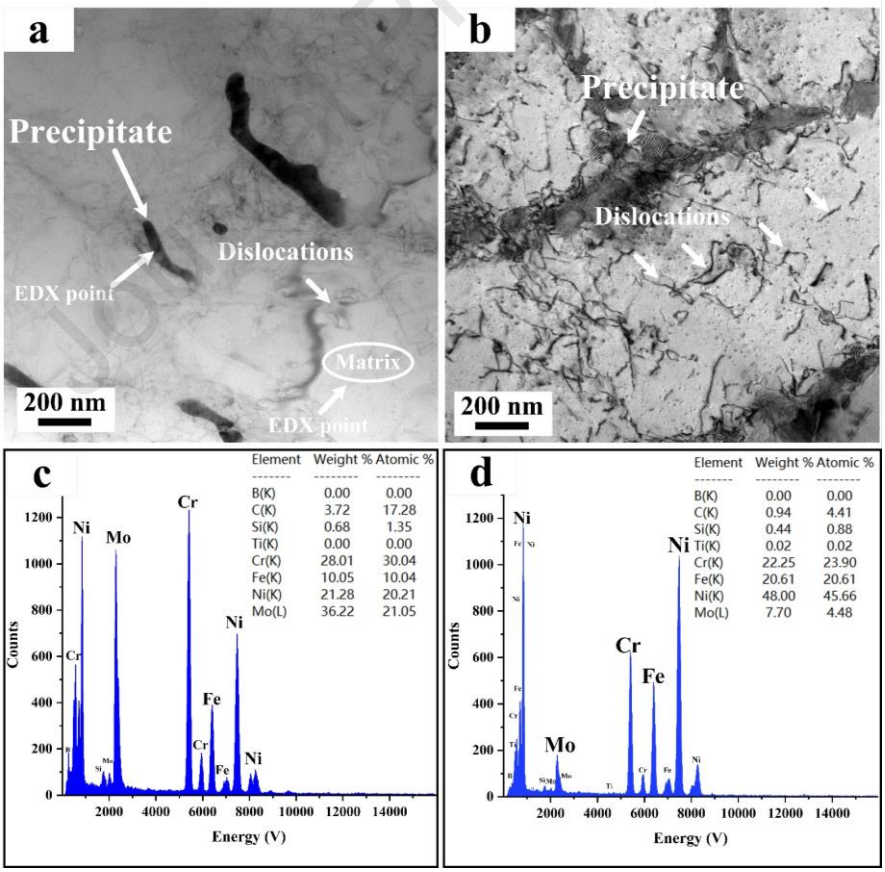


**Fig. 7.** Bright-field transmission electron microscope (TEM) images for the pure HX and HX-2 wt.% $TiB_2$ composite samples: (a) bright-field TEM image of the pure HX sample; (b) bright-field TEM image of the HX-2 wt.% $TiB_2$ composite sample; (c) EDX point analysis for the precipitate in Fig.7a; (d) EDX point analysis for the matrix in Fig.7a.

The typical austenite diffraction pattern (Fig. 8b) was revealed by selected area electron diffraction (SAED) in the matrix region of the composite sample (Fig. 8a). To further confirm the composition of precipitate, EDX point scanning was conducted on the precipitate shown in Fig. 8a. The EDX point analysis indicated that Cr and Mo elements were enriched in precipitate (Fig. 8c). The TEM high-resolution image of precipitate after fast Fourier transform (FFT) changes (Fig. 8d) further confirmed that the precipitate was $M_{23}C_6$ carbide.

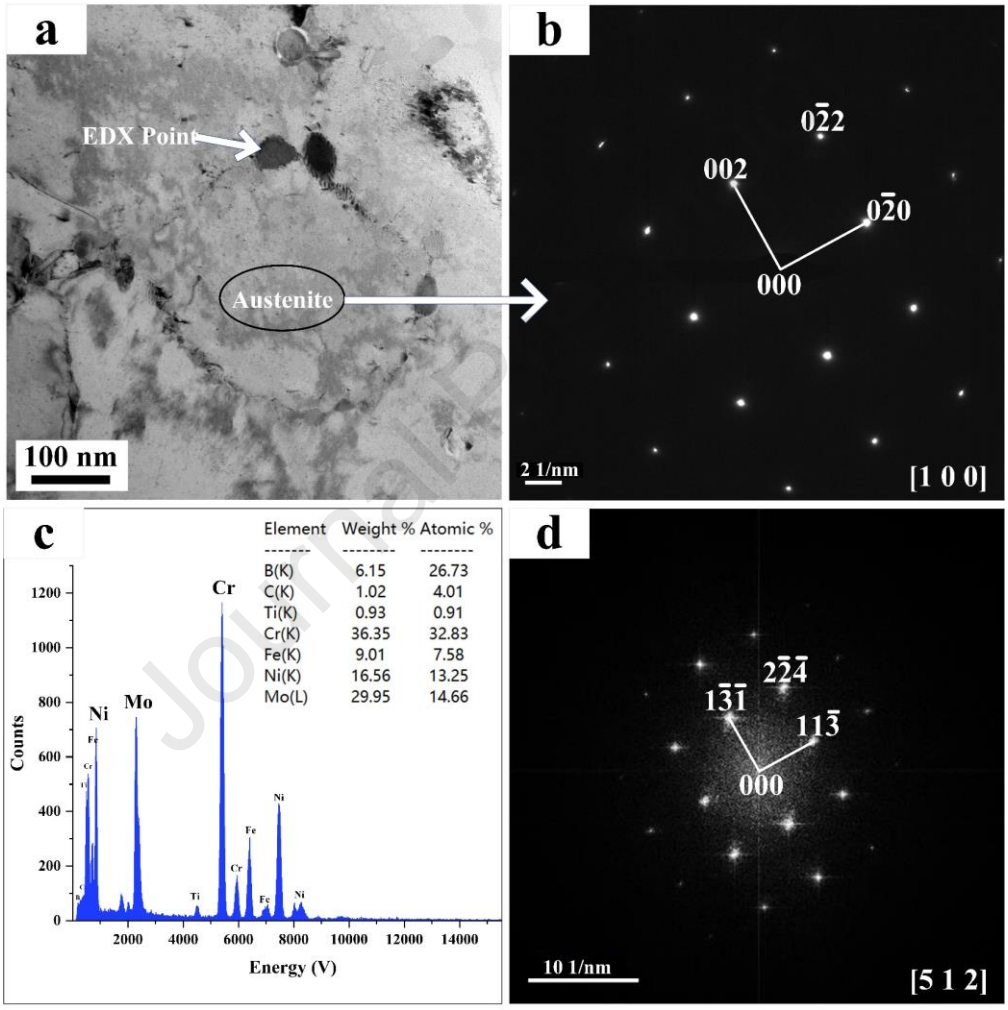


**Fig. 8.** Bright-field transmission electron microscope (TEM) images and selected area electron diffraction (SAED) patterns for the HX-2 wt.% $TiB_2$ composite sample: (a) bright-field TEM image of matrix and precipitate; (b) SAED pattern for the select matrix zone with zone axis [100]; (c) EDX point analysis for the precipitate; (d) high-resolution pattern converted by fast Fourier transform (FFT) for the selected EDX point area with zone axis [512].

The selected area's high-resolution pattern converted by fast Fourier transform (FFT) (Fig. 9c) further confirmed that the selected area was $TiB_2$

rather than other phases. In general, the $TiB_2$ particles embedded in the matrix can form a strong interface with the matrix (Figs. 9a and b), which aids in bearing the load and also strengthens the mechanical properties of the composite sample [38]. The interface quality is a significant indicator for evaluating the effects of the reinforcement phase on the LPBF-fabricated composites.

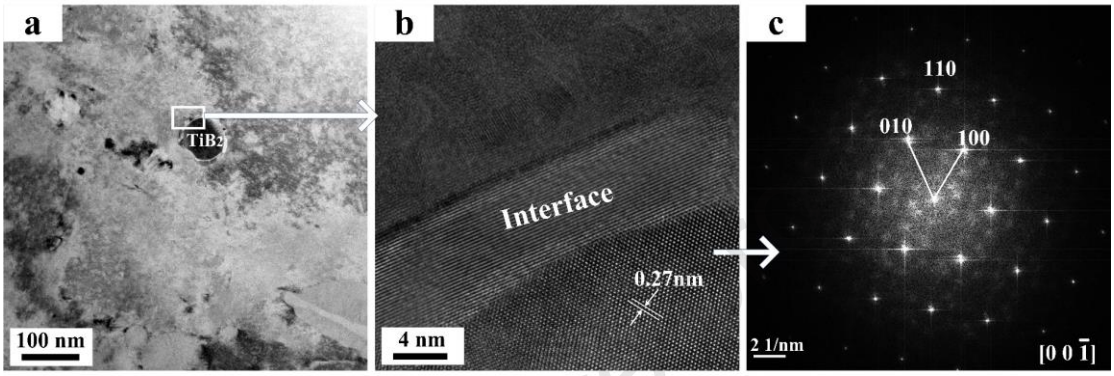


**Fig. 9.** Bright-field TEM images and SAED patterns for the HX-2 wt.% $TiB_2$ composite sample: (a) bright-field TEM image, including $TiB_2$; (b) high-resolution pattern of the selected area in Fig. 8a; (c) selected area high-resolution pattern converted by FFT with zone axis $[00\bar{1}]$.

Fig. 10, which shows EBSD images of pure HX and composite samples, reveals the changes in grain size and crystallographic orientation after the addition of 2 wt.% $TiB_2$ particles. The grain size of pure HX was noted to be larger than that of the composite sample; the columnar grains were dominant in pure HX, while numerous nearly equiaxial grains formed in the as-fabricated composite sample (Figs. 10a and c). The grain grew along the build direction in both samples. Obvious cracks were detected in pure HX, however, and were distributed along the grain boundaries, which confirmed that the cracks in HX were intergranular cracks rather than trans-granular cracks. No cracks were found on the grain boundary in the composite sample, but the grains were found to be refined (Figs. 10c–d). The number and size of the columnar grains decreased in the composite sample, indicating that $TiB_2$ played a significant role in heterogeneous nucleation and grain refinement.

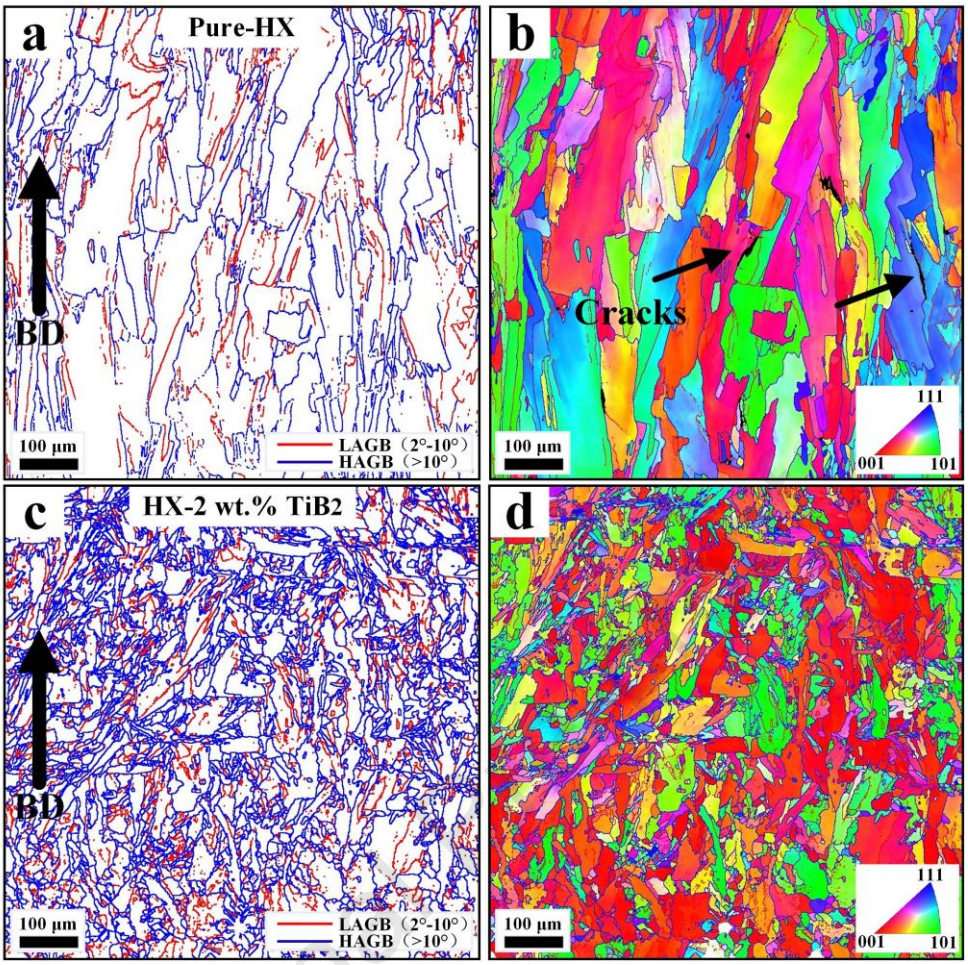


**Fig. 10.** Electron backscattered diffraction (EBSD) image of pure HX and HX-2 wt.% $TiB_2$ composite samples: (a) EBSD image quality map with high-angle and low-angle grain boundaries (HAGBs and LAGBs) superimposed for pure HX; (b) Inverse pole figure (IPF) orientation map for pure HX; (c) EBSD image quality map with HAGBs and LAGBs superimposed for the HX-2 wt.% $TiB_2$ composite sample; (d) IPF orientation map for HX-2 wt.% $TiB_2$ composite sample.

ImageJ software was used to count the proportion of the different grain boundaries in both samples (Fig. 10). Both low-angle grain boundaries (LAGBs) and high-angle grain boundaries (HAGBs) were indicated in the EBSD grain boundary images (Figs. 10a and c). The proportion of LAGBs in the pure HX sample was determined by the ratio of the area of red lines (Fig. 10a) to the area of the whole image. The LAGBs in the pure HX sample were found to account for 5.77% of the whole picture, while the HAGBs accounted for 11.04%. In the composite sample, LAGBs were determined to account for 9.9% of the whole picture, while the HAGBs occupied 29.71%.

Combined with the statistical grain aspect ratio distribution shown in Fig. 11,

the fraction of grains with aspect ratio less than 2 was up to 56.9% for the composite, while the value for pure HX was only 44.8%. Also, around 4.7% grains with aspect ratio greater than 9 were formed in pure HX, while they were not detected in the composite sample. A higher aspect ratio generally indicates a more columnar shaped grain. Therefore, the aspect ratio distribution analysis confirms that more fine and less columnar shaped grains were formed in the composite compared to the pure HX. Based on the statistical analysis of grain size, the average grain size was noted to have been reduced from 14 μm in the as-fabricated pure HX to 8.69 μm for the composite sample.

In conclusion, both LAGBs and HAGBs increased in the as-fabricated composite sample. The increased dislocations and fine grains may have had a significant impact on the mechanical performance of the composite material, as will be discussed in the next section.

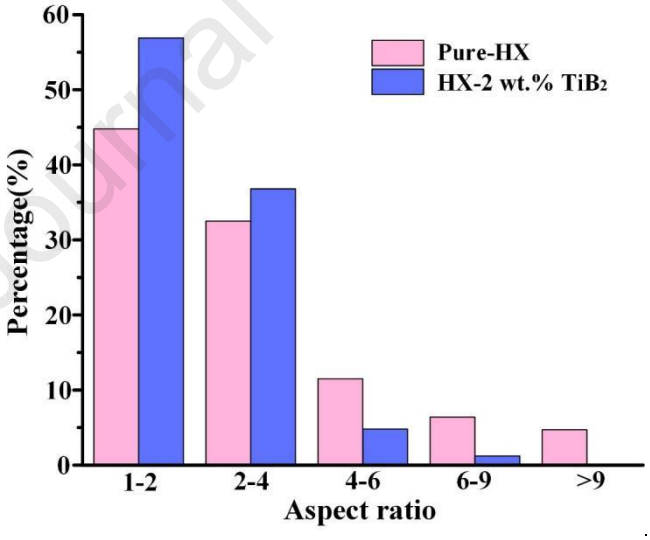


**Fig. 11.** Grain aspect ratio distribution of the pure HX and HX-2 wt.% $TiB_2$ composite.

As observed in the inverse pole figure (IPF) orientation map (Figs. 10b and d), the composite sample exhibited a stronger preferred orientation than the pure HX. The EBSD pole figures shown in Fig. 12 reveal the difference in crystallographic orientation between pure HX and composite samples. The pure HX seemed to exhibit a uniform texture, with a maximum texture density

of 4.79. Despite the grain refinement induced by the 2 wt.% $TiB_2$ particles, the composite sample tended to exhibit a strong (100) texture with a maximum density of 12.73. Future work should investigate the effects of $TiB_2$ particles (e.g. size and content) on the crystallographic orientation in LPBF-fabricated composites.

**Table 1**: Grain diameter statistical data for both samples.

| | **Pure-HX** | **HX-2 wt% $TiB_2$** |
|---|---|---|
| Equivalent average grain diameter | 14.015 μm | 8.6936 μm |
| Standard deviation | 26.228 μm | 10.897 μm |
| Coefficient of variation | 1.87 | 1.25 |
| Size of the data set | 917 | 4,186 |

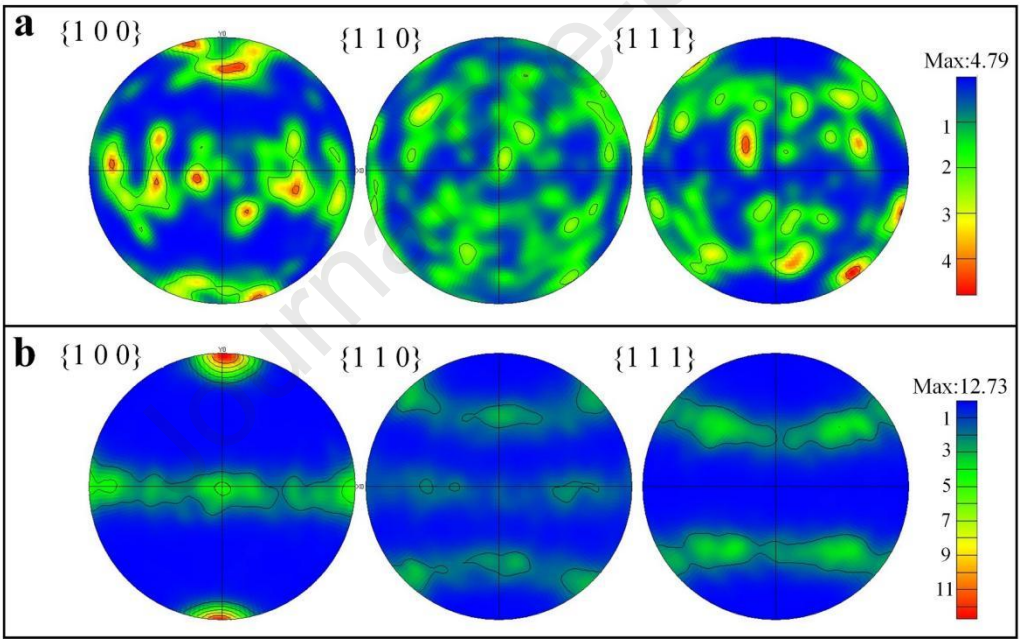


**Fig. 12.** Pole figures for the two samples: (a) pure HX sample; (b) HX-2 wt.% TiB2 composite sample.

### 3.3 Hardness analysis

Fig. 13 shows the room-temperature hardness and high-temperature (850 $^{o}$C) hardness of the pure HX and HX-2 wt.% $TiB_2$ composite samples (respectively) formed under optimal manufacturing parameters. The hardness data were obtained by taking an average of five points in different locations of each sample. The composite sample was much harder than the pure HX sample at both room temperature and high temperature. The average hardness of pure

HX and composite samples at room temperature was measured to be 265 HV and 380 HV, respectively.

It is not surprised that, due to the severe grain boundaries slip, both materials exhibited a reduction in hardness value at elevated temperatures compared to room temperature. The average hardness of pure HX and composite samples at 850 °C was measured to be 197 HV and 297 HV, respectively, indicating that the addition of $TiB_2$ contributed to the hardness of LPBF-formed samples increasing by 43.4% at room temperature and 50.8% at elevated temperature, respectively. This increase may have been due to grain refinement and the pinning effect of submicrometer $TiB_2$ particles on the grain boundaries. Our previous EBSD results (Figs. 10–11) demonstrated that the composite sample was significantly refined and the number of boundaries was much higher than that of pure HX. It may be noted that the added $TiB_2$ reinforcement was more influential to the mechanical property enhancement at high-temperature compared to the room temperature, the LPBF fabricated advanced HX-$TiB_2$ composite is thus expected to have significant potential applications in aero-engine domain.

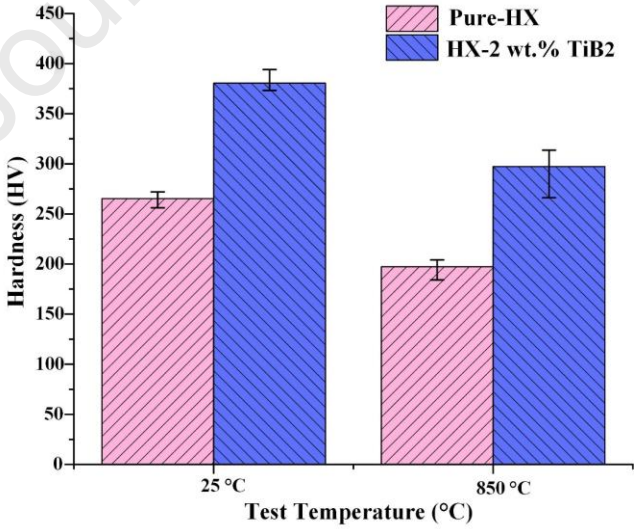


**Fig. 13.** The hardness of pure HX and HX-2 wt.% $TiB_2$ at different temperatures.

### 3.4 Tensile performance

As Fig. 14a shows, the yield strength of the as-fabricated HX alloy under the optimal process parameters was 555.9 ± 8.45 MPa, and the UTS was 692.5 ±

3.5 MPa at room temperature. The tensile behaviour of the two HX-2 wt.% $TiB_2$ composite specimens was found to be consistent, with a 715.5 ± 30.5 yield strength and a 1053.2 ± 19.6 MPa UTS. Both the yield strength and UTS of the HX-2 wt.% $TiB_2$ composite were significantly improved. This increased performance could also be attributed to $TiB_2$ induced grain refinement and the elimination of cracks. The pure HX exhibited an average 6.1 ± 0.3% elongation, which was slightly lower than the composite samples (7.26 ± 0.1%), indicating that the addition of 2 wt.% submicrometer $TiB_2$ particles did not cause a significant change in the ductility although the microcracks have been eliminated in the as-fabricated composite samples.

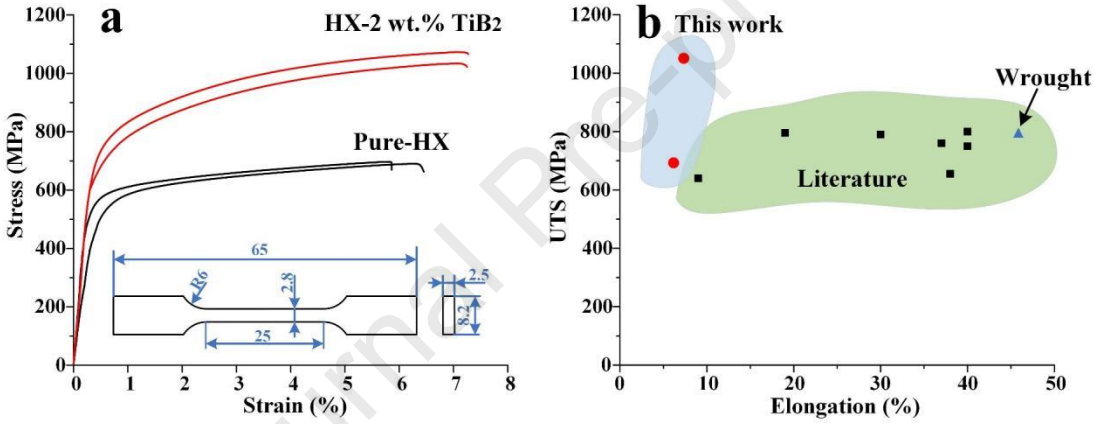


**Fig. 14.** Tensile performance of the as-fabricated pure HX and HX-2 wt.% $TiB_2$ composite samples: (a) engineering stress-strain curves of pure HX and HX-2 wt.% $TiB_2$ obtained in this work; (b) ultimate tensile strength (UTS) versus 'elongation to failure' values for HX alloy reported in the literature [39][40].

As Fig. 14 b shows, compared with previous studies on the tensile properties of HX alloy with different processing methods and post-treatment methods, the composite sample in this work was found to have the highest tensile strength, but the ductility after fracturing was sacrificed. A few possible reasons for this phenomenon are as follows. First, this situation may have been associated with the build direction of LPBF. Previous research has shown that vertically built samples (with a build direction parallel to the loading direction) exhibited an optimised combination of strength and ductility, but horizontal samples exhibited higher ultimate strength and lower ductility [33]. Second, the tensile strength and ductility of the HX alloy are related not only to

the processing method but also to the carbon content. A higher carbon content normally induces increased strength, with less elongation. Compared with the wrought HX samples, the fracture elongation of both pure HX and composite samples in the present work was lower than that of the wrought HX samples, but the UTS of the composite sample was over 200 MPa higher than that of wrought HX.

The elimination of residual pores may further improve the mechanical performance of the as-fabricated HX-2 wt.% $TiB_2$ composite samples. Previous studies have shown that hip isostatic processing (HIP) is an effective method to eliminate the pores in LPBF manufactured samples [41][42][43]. For instance, Han et al. [41] reported that relative density of LPBF samples increased from 99.3% to 99.98% after HIP post-treatment, both the cracks and gas-free micropores were eliminated. But HIP caused grain growth and coarseness, leading to the degradation of yield strength. Our future work aims to optimise the HIP process to balance both the strength and ductility properties of the LPBF fabricated HX-2 wt.% $TiB_2$ composite.

Fig. 15 shows the fracture morphology of two kinds of tensile samples, which confirms the mechanical properties' enhancement of the HX-2 wt.% $TiB_2$ composite. In a comparison of Figs. 15a and d, the pure HX fracture surface has more obvious defects. The pure-HX fracture surface showed many opened cracks (about 100 μm in length), as shown in Fig. 15b. These internal defects acted as stress concentration zones and induced fracture failure. Only a few small pores were found on the fracture surface of the composite specimen, with no obvious cracks detected. Therefore, the existence of fewer internal defects in the composite sample was important for strength improvement compared with pure HX.

About the same number of fine dimples were detected on the composite sample fracture surface, indicating that the same ductility between both materials (Figs. 15c and f). This finding was consistent with the previous experimental data, which showed that no significant improvement in ductility

was detected in the composite samples.

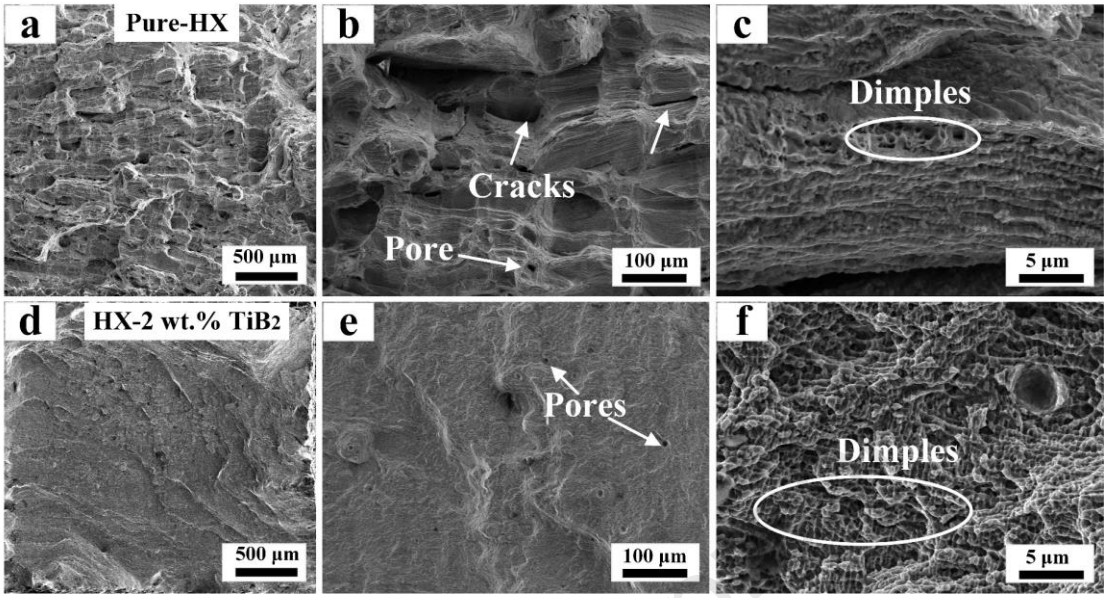


**Fig. 15.** SEM images showing the fracture surfaces of as-fabricated samples: (a)–(c): pure HX; (d)–(f): HX-2 wt.% $TiB_2$.

## 4 Discussion

### 4.1 Effects of $TiB_2$ addition on physical properties of composite powder

Previous study demonstrated that the physical properties of composite powder feedstock could be affected by the addition of enhanced ceramic particles [44]. In particular, the laser absorption and thermal conductivity for the composite powder cannot be ignored because they were closely related to the processability when the materials were processed via LPBF process.

It was reported that the laser absorption rate of particle reinforced composite powder could be significantly improved when the reinforced ceramic particles were attached to the surfaces of the metallic powder. The attached fine particles enabled rougher surfaces compared to unreinforced metallic powder, thereby increasing the laser-absorption rate [45]. The added ceramic particles reduced the thermal conductivity, whether their thermal conductivity is higher or lower than the matrices, because the ceramic particles covered the surface of the metal powder and introduced interfacial thermal resistance [46][44], leading to a higher laser-energy density needed to fully melt the composite

powder. Considering that the optimal laser-energy density reduced after the addition of $TiB_2$ particles in present study, this is very likely due to the addition of $TiB_2$, which changed the laser-absorption rate and effective thermal conductivity. The ImageJ software was used to calculate the proportion of unmelted particles under lower laser-energy density values and found that the proportion of the unmelted area in pure HX (Fig. 2c) and HX-2 wt.% $TiB_2$ composite (Fig. 2d) was 3.15% and 1.58%, respectively. In other words, Under the same laser energy density employed, the unmelted area in HX-2 wt.% $TiB_2$ composite sample was much smaller, indicating that the laser absorption rate improved and the composite powder was more fully melted after the addition of 2 wt.% $TiB_2$.

Previous research has shown that nano-TiC particles enabled the HX powder surface rougher and increased the laser-absorption rate, however, HX powder was coated by the nano-TiC particles and reduced the heat transfer due to the low thermal conductivity of TiC. The optimal laser-energy density for the HX-TiC composite was examined to be higher than that of pure HX [11]. The present study, however, revealed that the optimal laser-energy density for HX-2 wt.% $TiB_2$ composite was lower than that of pure HX, suggesting that the addition of $TiB_2$ was more influential to laser absorption rate compared to the effective thermal conductivity.

### 4.2 Possible microcrack elimination mechanism

The results in this study reveal that cracks were generated in the pure HX regardless of the laser-energy density. It is challenging to eliminate the microcracks by optimising the laser energy density. Also, the experimental results in this study showed that all cracks in pure HX were intergranular cracks and no transgranular cracks were detected. This may indicate that the grain boundaries are sensitive to cracking. Previous study has shown that cracks in LPBF HX are mainly caused by the combined action of carbides distributed along grain boundaries and residual thermal stress [3]. In this study,

Cr and Mo enriched carbide precipitates were found in both pure HX and HX-2 wt.% $TiB_2$ composite samples. This kind of carbide with low melting point is considered to be one of the main contributors for the crack formation of HX alloy in the process of LPBF [25]. The melting point of carbide is lower than the matrix, liquid film could be formed during the solidification process. Under the action of residual thermal stress, liquid films may be pulled apart, leading to the crack formation.

Compared to pure HX, the elimination of microcracks was achieved by adding submicrometer $TiB_2$ particles in this research. Cr and Mo enriched carbides were also found in the crack-free composite samples in this study, indicating that the addition of $TiB_2$ particles could not inhibit precipitation. This suggests that the elimination of cracks in composite may be due to the reduction of residual thermal stress. Our EBSD results revealed that the grains formed in composite sample were smaller than those in the pure HX sample, so that the grain boundaries increased significantly after grain refinement. (Fig. 10). An increase in the number of grain boundaries helps share the residual stress, which prevents cracking at the grain boundaries. Also, the formed strong interfacial connection between $TiB_2$ particles and matrix (Fig. 9) also strengthens the grain boundary to resist thermal stress to avoid cracking.

### 4.3 Possible strengthening mechanisms

The experimental results in this study have shown that the addition of 2 wt.% $TiB_2$ particles in Ni-based HX alloy could eliminate the cracks and improve the mechanical properties. The available research results from literature indicate that the possible mechanisms in strength improvement by the introduction of reinforcement particles include the Orowan strengthening, grain size strengthening, load-bearing and enhanced dislocation density strengthening [47][48][49]. The Orowan strengthening increases with a decrease in the reinforced particle size, and it becomes dominant when the particle size reaches the nanometer scale [50]. The $TiB_2$ used in this study is

submicrometer scale (average particle size = 600 nm, with several particles greater than 1 μm), therefore the Orowan strengthening may not be the primary contributor for mechanical performance enhancement for the composite in this study.

The grain size strengthening is mainly due to grain refinement. Since a significant increase in grain boundaries detected in the HX-2 wt.% $TiB_2$ composite, where the grain boundary fraction increased from 16.81% for the pure HX to 39.61% for the composite. The grain boundaries may hinder the movement of dislocations during the stretching process to enhance the yield strength and hardness of the composite at room temperature.

Since strong interfaces formed between $TiB_2$ particles and the austenite matrix, another factor that could not be neglected is the load-bearing strengthening. The load-bearing strengthening can be estimated using the formula [51]: $\Delta\sigma_{Load} = 1/2\, v_p \sigma_m$, where $v_p$ is the volume fraction of the particles, $\sigma_m$ is the yield strength of the matrix. In this study, the estimated $\Delta\sigma_{Load}$ is determined to be over 100 MPa, indicating the load-bearing strengthening is a significant mechanism in the LPBF fabricated HX-2 wt.% $TiB_2$ composite. In addition, the LAGBs was increased from 5.77% to 9.9% in the composite sample, suggesting the enhanced dislocation density strengthening is also a non-negligible strengthening mechanism in the as-fabricated composite.

## 5 Conclusions

This research has revealed a novel method of manufacturing crack-free and high-strength Hastelloy-X (HX) alloy by laser powder bed fusion (LPBF) additive manufacturing process. According to the above experimental results, the following conclusions may be drawn:

(1) The optimal laser-energy densities for manufacturing pure HX and the HX-2 wt.% $TiB_2$ composite were determined to be 125 and 89.3 J/mm$^3$, respectively. This finding suggests that the addition of $TiB_2$ particles greatly

improved the laser absorptivity of the powder material, such that a lower laser-energy density was needed to manufacture the full-density HX-2 wt.% $TiB_2$ composite samples.

(2) The addition of submicrometer $TiB_2$ particles was found to eliminate the cracks in the LPBF additive-manufactured samples. The addition of $TiB_2$ did not prevent the formation of segregated carbides. This finding indicates the elimination of cracks may be due to the reduction of residual stress.

(3) Compared with pure HX, the room-temperature hardness and high-temperature hardness of the HX-2 wt.% $TiB_2$ composite increased by 43.4% and 50.8%, respectively. The addition of 2 wt.% $TiB_2$ submicrometer particles also contributed to a 28% increase in yield strength. This finding suggests that the added 2 wt.% $TiB_2$ could improve both the room-temperature and high-temperature mechanical properties, which is of great significance for applications in aero-engine components.

Our research has proved that the addition of 2 wt.% $TiB_2$ submicrometer particles to HX powder can eliminate the microcracks in the LPBF of HX alloy; doing so also improves the material's mechanical properties under both room- and high-temperature conditions. The findings may speed the application of LPBF additive manufacturing in HX superalloys and may also provide a reference for the additive manufacturing of other cracking-sensitive alloys. Researchers should note, however, that the HX-2 wt.% $TiB_2$ composite material exhibited a stronger (100) texture compared to pure HX, which may have caused anisotropy among the fabricated specimens. Future work should thus further study the effects of $TiB_2$ content on the crystallographic orientation of LPBF-fabricated materials.

## Acknowledgements

This work was supported by the National Natural Science Foundation of China (Grant No. 52005295), Shenzhen Science and Technology Program (Grant No. RCBS20200714114921323) and the Major basic research projects of

Shandong Natural Science Foundation of China (Grant No. ZR2020ZD05).

## CRediT authorship contribution statement

**Zhenhua Zhang:** Conceptualization, Methodology, Writing-original draft. **Quanquan Han:** Conceptualization, Investigation, Writing - Original Draft, Funding acquisition. **Shengzhao Yang:** Resources, Writing - Review & Editing.

**Yingyue Yin：**Visualization, Data curation. **Jian Gao:** Software, Investigation.

**Rossitza Setchi:** Methodology, Review & Editing.

## Declaration of interest statement

The authors have no conflict of interest.

## Data availability statement

The raw/processed data required to reproduce these findings cannot be shared at this time as the data also forms part of an ongoing study.

## References

[1] J.-C. Zhao, M. Larsen, V. Ravikumar, Phase precipitation and time–temperature-transformation diagram of Hastelloy X, Mater. Sci. Eng. A. 293 (2000) 112–119. https://doi.org/10.1016/S0921-5093(00)01049-2.

[2] F. Wang, X.H. Wu, D. Clark, On direct laser deposited Hastelloy X: dimension, surface finish, microstructure and mechanical properties, Mater. Sci. Technol. 27 (2011) 344–356. https://doi.org/10.1179/026708309X12578491814591.

[3] G. Marchese, G. Basile, E. Bassini, A. Aversa, M. Lombardi, D. Ugues, P. Fino, S. Biamino, Study of the Microstructure and Cracking Mechanisms of Hastelloy X Produced by Laser Powder Bed Fusion, Materials (Basel). 11 (2018) 106. https://doi.org/10.3390/ma11010106.

[4] F. Wang, Mechanical property study on rapid additive layer manufacture Hastelloy® X alloy by selective laser melting technology, Int. J. Adv. Manuf. Technol. 58 (2012) 545–551. https://doi.org/10.1007/s00170-011-3423-2.

[5] M.L. Montero-Sistiaga, Z. Liu, L. Bautmans, S. Nardone, G. Ji, J.-P. Kruth, J. Van Humbeeck, K. Vanmeensel, Effect of temperature on the microstructure and tensile properties of micro-crack free hastelloy X produced by selective laser melting, Addit. Manuf. 31 (2020) 100995. https://doi.org/10.1016/j.addma.2019.100995.

[6] D.D. Gu, W. Meiners, K. Wissenbach, R. Poprawe, Laser additive manufacturing of metallic components: materials, processes and mechanisms, Int. Mater. Rev. 57 (2012) 133–164. https://doi.org/10.1179/1743280411Y.0000000014.

[7] D. Herzog, V. Seyda, E. Wycisk, C. Emmelmann, Additive manufacturing of metals, Acta Mater. 117 (2016) 371–392. https://doi.org/10.1016/j.actamat.2016.07.019.

[8] F. Trevisan, F. Calignano, A. Aversa, G. Marchese, M. Lombardi, S. Biamino, D. Ugues, D. Manfredi, Additive manufacturing of titanium alloys in the biomedical field: processes, properties and applications., J. Appl. Biomater. Funct. Mater. 16 (2018) 57–67. https://doi.org/10.5301/jabfm.5000371.

[9] A.B. Badiru, V. V. Valencia, D. Liu, Additive manufacturing: Handbook product development for the defense industry, 2017. https://doi.org/10.1201/9781315119106.

[10] Q. Han, Y. Gu, S. Soe, F. Lacan, R. Setchi, Effect of hot cracking on the mechanical properties of Hastelloy X superalloy fabricated by laser powder bed fusion additive manufacturing, Opt. Laser Technol. 124 (2020) 105984. https://doi.org/10.1016/j.optlastec.2019.105984.

[11] Q. Han, Y. Gu, L. Wang, Q. Feng, H. Gu, R. Johnston, R. Setchi, Effects of TiC content on microstructure and mechanical properties of nickel-based hastelloy X nanocomposites manufactured by selective laser melting, Mater. Sci. Eng. A. 796 (2020) 140008. https://doi.org/10.1016/j.msea.2020.140008.

[12] A. Keshavarzkermani, E. Marzbanrad, R. Esmaeilizadeh, Y. Mahmoodkhani, U. Ali, P.D. Enrique, N.Y. Zhou, A. Bonakdar, E. Toyserkani, An investigation into the effect of process parameters on melt pool geometry, cell spacing, and grain refinement during laser powder bed fusion, Opt. Laser Technol. 116 (2019) 83–91. https://doi.org/10.1016/j.optlastec.2019.03.012.

[13] O. Sanchez-Mata, X. Wang, J. Muñiz-Lerma, M. Attarian Shandiz, R. Gauvin, M. Brochu, Fabrication of Crack-Free Nickel-Based Superalloy Considered Non-Weldable during Laser Powder Bed Fusion, Materials (Basel). 11 (2018) 1288. https://doi.org/10.3390/ma11081288.

[14] D. Tomus, P.A. Rometsch, M. Heilmaier, X. Wu, Effect of minor alloying elements on crack-formation characteristics of Hastelloy-X manufactured by selective laser melting, Addit. Manuf. 16 (2017) 65–72. https://doi.org/10.1016/j.addma.2017.05.006.

[15] E. Chauvet, P. Kontis, E.A. Jägle, B. Gault, D. Raabe, C. Tassin, J.J. Blandin, R. Dendievel, B. Vayre, S. Abed, G. Martin, Hot cracking mechanism affecting a non-weldable Ni-based superalloy produced by selective electron Beam Melting, Acta Mater. 142 (2018) 82–94. https://doi.org/10.1016/j.actamat.2017.09.047.

[16] N.J. Harrison, I. Todd, K. Mumtaz, Reduction of micro-cracking in nickel superalloys processed by Selective Laser Melting: A fundamental alloy design approach, Acta Mater. 94 (2015) 59–68. https://doi.org/10.1016/j.actamat.2015.04.035.

[17] J.H. Martin, B.D. Yahata, J.M. Hundley, J.A. Mayer, T.A. Schaedler, T.M. Pollock, 3D printing of high-strength aluminium alloys, Nature. 549 (2017) 365–369. https://doi.org/10.1038/nature23894.

[18] D. Gu, F. Chang, D. Dai, Selective Laser Melting Additive Manufacturing of Novel Aluminum Based Composites With Multiple Reinforcing Phases, J. Manuf. Sci. Eng. 137 (2015). https://doi.org/10.1115/1.4028925.

[19] R. Casati, M. Vedani, Metal Matrix Composites Reinforced by Nano-Particles—A Review, Metals (Basel). 4 (2014) 65–83. https://doi.org/10.3390/met4010065.

[20] Q. Han, Y. Gu, H. Gu, Y. Yin, J. Song, Z. Zhang, S. Soe, Laser powder bed fusion of

WC-reinforced Hastelloy-X composite: microstructure and mechanical properties, J. Mater. Sci. 56 (2021) 1768–1782. https://doi.org/10.1007/s10853-020-05327-6.

[21] B. Zhang, G. Bi, S. Nai, C.N. Sun, J. Wei, Microhardness and microstructure evolution of TiB2 reinforced Inconel 625/TiB2 composite produced by selective laser melting, Opt. Laser Technol. 80 (2016) 186–195. https://doi.org/10.1016/j.optlastec.2016.01.010.

[22] X. Zhao, Q.S. Wei, N. Gao, E.L. Zheng, Y.S. Shi, S.F. Yang, Rapid fabrication of TiN/AISI 420 stainless steel composite by selective laser melting additive manufacturing, J. Mater. Process. Technol. 270 (2019) 8–19. https://doi.org/10.1016/j.jmatprotec.2019.01.028.

[23] P. Wang, B. Zhang, C.C. Tan, S. Raghavan, Y.F. Lim, C.N. Sun, J. Wei, D. Chi, Microstructural characteristics and mechanical properties of carbon nanotube reinforced Inconel 625 parts fabricated by selective laser melting, Mater. Des. 112 (2016) 290–299. https://doi.org/10.1016/j.matdes.2016.09.080.

[24] D. Turnbull, B. Vonnegut, Nucleation Catalysis., Ind. Eng. Chem. 44 (1952) 1292–1298. https://doi.org/10.1021/ie50510a031.

[25] Q. Han, Y. Gu, R. Setchi, F. Lacan, R. Johnston, S.L. Evans, S. Yang, Additive manufacturing of high-strength crack-free Ni-based Hastelloy X superalloy, Addit. Manuf. 30 (2019) 100919. https://doi.org/10.1016/j.addma.2019.100919.

[26] Q. Han, Y. Gu, J. Huang, L. Wang, K.W.Q. Low, Q. Feng, Y. Yin, R. Setchi, Selective laser melting of Hastelloy X nanocomposite: Effects of TiC reinforcement on crack elimination and strength improvement, Compos. Part B Eng. 202 (2020) 108442. https://doi.org/10.1016/j.compositesb.2020.108442.

[27] S. Shimada, M. Kozeki, Oxidation of TiC at low temperatures, J. Mater. Sci. 27 (1992) 1869–1875. https://doi.org/10.1007/BF01107214.

[28] W.G. Fahrenholtz, G.E. Hilmas, Oxidation of ultra-high temperature transition metal diboride ceramics, Int. Mater. Rev. 57 (2012) 61–72. https://doi.org/10.1179/1743280411Y.0000000012.

[29] W. Li, Y. Yang, J. Liu, Y. Zhou, M. Li, S. Wen, Q. Wei, C. Yan, Y. Shi, Enhanced nanohardness and new insights into texture evolution and phase transformation of TiAl/TiB 2 in-situ metal matrix composites prepared via selective laser melting, Acta Mater. 136 (2017) 90–104. https://doi.org/10.1016/j.actamat.2017.07.003.

[30] Z. Fan, Y. Wang, Y. Zhang, T. Qin, X.R. Zhou, G.E. Thompson, T. Pennycook, T. Hashimoto, Grain refining mechanism in the Al/Al–Ti–B system, Acta Mater. 84 (2015) 292–304. https://doi.org/10.1016/j.actamat.2014.10.055.

[31] R.G. Munro, Material properties of titanium diboride, J. Res. Natl. Inst. Stand. Technol. 105 (2000) 709. https://doi.org/10.6028/jres.105.057.

[32] B.L. Bramfitt, The effect of carbide and nitride additions on the heterogeneous nucleation behavior of liquid iron, Metall. Trans. 1 (1970) 2958. https://doi.org/10.1007/BF03037838.

[33] K. Guan, Z. Wang, M. Gao, X. Li, X. Zeng, Effects of processing parameters on tensile properties of selective laser melted 304 stainless steel, Mater. Des. 50 (2013) 581–586. https://doi.org/10.1016/j.matdes.2013.03.056.

[34] C. Qiu, N.J.E. Adkins, M.M. Attallah, Selective laser melting of Invar 36: Microstructure and properties, Acta Mater. 103 (2016) 382–395.

https://doi.org/10.1016/j.actamat.2015.10.020.

[35] U. Scipioni Bertoli, A.J. Wolfer, M.J. Matthews, J.-P.R. Delplanque, J.M. Schoenung, On the limitations of Volumetric Energy Density as a design parameter for Selective Laser Melting, Mater. Des. 113 (2017) 331–340. https://doi.org/10.1016/j.matdes.2016.10.037.

[36] C. Zhao, N.D. Parab, X. Li, K. Fezzaa, W. Tan, A.D. Rollett, T. Sun, Critical instability at moving keyhole tip generates porosity in laser melting, Science (80-. ). 370 (2020) 1080–1086. https://doi.org/10.1126/science.abd1587.

[37] C. Ma, J. Zhao, C. Cao, T.-C. Lin, X. Li, Fundamental Study on Laser Interactions With Nanoparticles-Reinforced Metals—Part II: Effect of Nanoparticles on Surface Tension, Viscosity, and Laser Melting, J. Manuf. Sci. Eng. 138 (2016). https://doi.org/10.1115/1.4033446.

[38] G. Garces, G. Bruno, A. Wanner, Load transfer in short fibre reinforced metal matrix composites, Acta Mater. 55 (2007) 5389–5400. https://doi.org/10.1016/j.actamat.2007.06.003.

[39] M.L. Montero-Sistiaga, S. Pourbabak, J. Van Humbeeck, D. Schryvers, K. Vanmeensel, Microstructure and mechanical properties of Hastelloy X produced by HP-SLM (high power selective laser melting), Mater. Des. 165 (2019) 107598. https://doi.org/10.1016/j.matdes.2019.107598.

[40] D. Tomus, Y. Tian, P.A. Rometsch, M. Heilmaier, X. Wu, Influence of post heat treatments on anisotropy of mechanical behaviour and microstructure of Hastelloy-X parts produced by selective laser melting, Mater. Sci. Eng. A. 667 (2016) 42–53. https://doi.org/10.1016/j.msea.2016.04.086.

[41] Q. Han, R. Mertens, M.L. Montero-Sistiaga, S. Yang, R. Setchi, K. Vanmeensel, B. Van Hooreweder, S.L. Evans, H. Fan, Laser powder bed fusion of Hastelloy X: Effects of hot isostatic pressing and the hot cracking mechanism, Mater. Sci. Eng. A. 732 (2018) 228–239. https://doi.org/10.1016/j.msea.2018.07.008.

[42] S. Tammas-Williams, P.J. Withers, I. Todd, P.B. Prangnell, The Effectiveness of Hot Isostatic Pressing for Closing Porosity in Titanium Parts Manufactured by Selective Electron Beam Melting, Metall. Mater. Trans. A. 47 (2016) 1939–1946. https://doi.org/10.1007/s11661-016-3429-3.

[43] Y.Y. Kaplanskii, E.A. Levashov, A. V. Korotitskiy, P.A. Loginov, Z.A. Sentyurina, A.B. Mazalov, Influence of aging and HIP treatment on the structure and properties of NiAl-based turbine blades manufactured by laser powder bed fusion, Addit. Manuf. 31 (2020) 100999. https://doi.org/10.1016/j.addma.2019.100999.

[44] W.H.H. Yu, S.L.L. Sing, C.K.K. Chua, C.N.N. Kuo, X.L.L. Tian, Particle-reinforced metal matrix nanocomposites fabricated by selective laser melting: A state of the art review, Prog. Mater. Sci. 104 (2019) 330–379. https://doi.org/10.1016/j.pmatsci.2019.04.006.

[45] C. Ma, J. Zhao, C. Cao, T.-C. Lin, X. Li, Fundamental Study on Laser Interactions With Nanoparticles-Reinforced Metals—Part I: Effect of Nanoparticles on Optical Reflectivity, Specific Heat, and Thermal Conductivity, J. Manuf. Sci. Eng. 138 (2016). https://doi.org/10.1115/1.4033392.

[46] J. Ordonez-Miranda, R. Yang, J.J. Alvarado-Gil, Thermal Conductivity of Particulate

Nanocomposites, in: 2014: pp. 93–139. https://doi.org/10.1007/978-3-319-02012-9_3.

[47] C.S. Kim, I. Sohn, M. Nezafati, J.B. Ferguson, B.F. Schultz, Z. Bajestani-Gohari, P.K. Rohatgi, K. Cho, Prediction models for the yield strength of particle-reinforced unimodal pure magnesium (Mg) metal matrix nanocomposites (MMNCs), J. Mater. Sci. 48 (2013) 4191–4204. https://doi.org/10.1007/s10853-013-7232-x.

[48] M. Habibnejad-Korayem, R. Mahmudi, W.J. Poole, Enhanced properties of Mg-based nano-composites reinforced with Al2O3 nano-particles, Mater. Sci. Eng. A. 519 (2009) 198–203. https://doi.org/10.1016/j.msea.2009.05.001.

[49] J.B. Ferguson, F. Sheykh-Jaberi, C.S. Kim, P.K. Rohatgi, K. Cho, On the strength and strain to failure in particle-reinforced magnesium metal-matrix nanocomposites (Mg MMNCs), Mater. Sci. Eng. A. 558 (2012) 193–204. https://doi.org/10.1016/j.msea.2012.07.111.

[50] Q.B. Nguyen, M. Gupta, Increasing significantly the failure strain and work of fracture of solidification processed AZ31B using nano-Al2O3 particulates, J. Alloys Compd. 459 (2008) 244–250. https://doi.org/10.1016/j.jallcom.2007.05.038.

[51] A. Sanaty-Zadeh, Comparison between current models for the strength of particulate-reinforced metal matrix nanocomposites with emphasis on consideration of Hall–Petch effect, Mater. Sci. Eng. A. 531 (2012) 112–118. https://doi.org/10.1016/j.msea.2011.10.043.

**Declaration of interests**

☒ The authors declare that they have no known competing financial interests or personal relationships that could have appeared to influence the work reported in this paper.

☐The authors declare the following financial interests/personal relationships which may be considered as potential competing interests: